



Co-delivery of curcumin and resveratrol by folic acid-conjugated poly (glycerol adipate) nanoparticles for enhanced synergistic anticancer effect against osteosarcoma

Amaraporn Wongrakpanich^a, Huong Bui Thi Thu^b, Krisada Sakchaisri^c, Vincenzo Taresco^d, Valentina Cuzzucoli Crucitti^e, Somnuk Bunsupa^f, Jiraphong Suksiriworapong^{a,*}

^a Department of Pharmacy, Faculty of Pharmacy, Mahidol University, Bangkok, 10400, Thailand

^b Department of Pharmacy, Faculty of Health, University of Angers, Angers, 49100, France

^c Department of Pharmacology, Faculty of Pharmacy, Mahidol University, Bangkok, 10400, Thailand

^d School of Chemistry, University of Nottingham, Nottingham, NG7 2RD, United Kingdom

^e Department of Chemical and Environment Engineering, University of Nottingham, Nottingham, NG7 2RD, United Kingdom

^f Department of Pharmacognosy, Faculty of Pharmacy, Mahidol University, Bangkok, 10400, Thailand

ARTICLE INFO

Keywords:

Curcumin
Resveratrol
Nanoparticle
Osteosarcoma
Co-delivery
Synergistic

ABSTRACT

This study explored the co-delivery of curcumin (CUR) and resveratrol (RV) using folic acid-conjugated poly (glycerol adipate)-based nanoparticles (FPPC NPs) to enhance their synergistic anticancer effects against osteosarcoma. Based on synergistic toxicity experiments against Saos-2 cells, the optimal synergistic CUR:RV ratios were 1:2 and 1:3, which were used for co-encapsulation. Increasing the amount of RV in the co-loaded NPs did not affect the properties of the nanocarriers, but predominantly increased the loading capacity of RV, especially at the 1:3 ratio, by 1.8–2.0 times, mediated by their interaction. All co-loaded NPs demonstrated sustained release of CUR with a burst release of RV, and the presence of RV accelerated the initial release of CUR from the carriers. Furthermore, the co-encapsulated NPs maintained CUR and RV synergism and greatly enhanced their toxicity against osteosarcoma by at least 1.8 times compared to their corresponding solutions through profound accumulation of Saos-2 cells in the sub G1 phase and late apoptosis. The internalization of FPPC NPs into cells via endocytosis was dose- and time-dependent. This study offers a proof-of-concept for a potential co-delivery system using tumor-targeted poly(glycerol adipate)-based NPs to enhance the anticancer activity of CUR and RV against osteosarcoma.

1. Introduction

Curcumin (CUR) and resveratrol (RV) are phytochemicals that exert anticancer activity against many cancers through various mechanisms [1,2]. CUR and RV have been investigated as potential anticancer drugs because of their unique benefits, including relative safety in humans, inhibition of various cellular pathways associated with tumor survival and progression, and suppression of chemoresistance in comparison to conventional chemotherapeutic agents [3–5]. CUR targets multiple chemotherapeutic pathways and inhibits cell growth in a dose-dependent manner in seven human osteosarcoma cell lines by inducing apoptosis and G2/M phase arrest [6,7]. Recent studies have suggested that RV also exhibits multiple tumor-suppressive activity in

osteosarcoma cells [8,9]. Emerging evidence has illustrated that CUR and RV exhibit synergism when individually combined with chemotherapeutic agents such as 5-fluorouracil, cisplatin, doxorubicin, paclitaxel, and oxaliplatin [2,5]. Further, the synergistic effects of CUR and RV in hepatocellular carcinoma [10], colorectal cancer [11,12], prostate cancer [13], and head and neck carcinomas [14,15] have been reported. This synergistic potential, coupled with their relative safety, makes them promising candidates for primary and adjunct therapy in osteosarcoma.

Traditional chemotherapeutic regimens rely on combining drugs with non-overlapping mechanisms of action; however, achieving an ideal ratio of these agents at the tumor site is crucial for therapeutic success [16,17]. Despite administering the correct dose of combination chemotherapy drugs into the systemic circulation, significant

* Corresponding author.

E-mail address: jiraphong.suk@mahidol.edu (J. Suksiriworapong).

<https://doi.org/10.1016/j.jddst.2024.105610>

Received 28 November 2023; Received in revised form 1 March 2024; Accepted 22 March 2024

Available online 23 March 2024

1773-2247/© 2024 The Authors. Published by Elsevier B.V. This is an open access article under the CC BY-NC-ND license (<http://creativecommons.org/licenses/by-nc-nd/4.0/>).

degradation and uncontrollable distribution may result in an inadequate drug ratio at the tumor site, hindering therapeutic efficacy and potentially worsening patient toxicity [18,19]. Another challenge in combination chemotherapy is harmonizing drug pharmacokinetics with cellular uptake [19,20]. Many patients develop drug-related side effects from standard chemotherapy for osteosarcoma, including doxorubicin, cisplatin, and high-dose methotrexate [21], leading to treatment discontinuation. Therefore, there is an urgent need to develop new and effective therapies with minimal adverse effects. A key strategy to improve the efficacy of combination therapies is the development of a more precise and controlled delivery system for multiple therapeutic candidates. Nanoparticles (NPs) are emerging as a promising platform to address these challenges because they can be engineered to deliver multiple drugs concurrently to targeted cells [22]. NPs can also be engineered to exert synergistic therapeutic effects and overcome chemotherapeutic drug resistance. Their success relies heavily on the carrier material, which plays a crucial role in modulating drug pharmacokinetics [23].

As previously mentioned, an effective ratio of CUR to RV in treating different cancers is crucial and may result in various outcomes. Moreover, the clinical translation of CUR and RV is limited by their poor pharmacokinetics and aqueous solubility properties [24,25]. NPs offer a solution for avoiding these limitations by unifying drug pharmacokinetics, thus enabling the concurrent delivery of multiple therapeutic agents in a precise and predefined ratio to achieve effective combination therapy. NPs have gained attention owing to their ability to co-encapsulate and deliver drugs to target diseased cells. In recent decades, CUR and RV have been co-delivered using various drug delivery systems, such as hyalurosomes, nanoparticles, liposomes, lipid nanocapsules, polymeric micelles, and dendrimers [13,26–35]. However, few studies have investigated this approach for cancer treatments [33–35]. Amphiphilic dendrimer NPs loaded with CUR and RV showed a slow drug release profile with improved cytotoxicity against the neuroblastoma cell line (SH-SY5Y) compared to the dual drug solution [35]. Alginate NPs with small particle sizes had entrapment efficiencies of 49.3% and 71.0% for CUR and RV, respectively. However, they exhibited lower toxicity against DU145 prostate cancer cells than their solutions [33]. Recently, hepatocellular carcinoma-targeted liposomes have been shown to be promising delivery systems for CUR and RV at a 1:5 ratio, providing improved bioavailability [34].

To the best of our knowledge, a combination of CUR and RV has never been established for the treatment of osteosarcoma; thus, the optimal synergistic ratio is yet to be elucidated. In addition, the use of tumor-targeted polymeric NPs for the co-delivery of an effective ratio of CUR to RV has not been investigated. Previously, we demonstrated successful folate receptor-targeted delivery of partially purified acetogenin-enriched extract using folic acid-conjugated polyethylene glycol-grafted cholesterol-modified poly(glycerol adipate) (FPPC) [36]. This polymer is a promising candidate for drug delivery applications because it is fabricated from biodegradable and biocompatible poly(glycerol adipate) (PGA), which is modified with cholesterol as the hydrophobic moiety [37]. Although several studies have demonstrated the success of modified PGAs in drug delivery applications [38–41], no reports on dual drug delivery using PGA-based NPs have been published to date. Building upon our prior success with targeted delivery using FPPC NPs, we extended this innovative platform to co-deliver CUR and RV in a precise, synergistic ratio. Therefore, this study aimed to concurrently deliver CUR and RV using folate receptor-targeted PGA-based NPs to achieve synergistic anticancer effects against Saos-2 osteosarcoma cells. The NPs were fabricated for the co-encapsulation of CUR and RV at their initially predetermined optimal ratios in comparison to their corresponding single drug-loaded NPs. Their physicochemical properties, release profiles, and physical stabilities were evaluated. Further, the *in vitro* synergistic anticancer effect, mechanism of drug-induced cell death, and cellular uptake of the NPs were assessed.

2. Materials and methods

2.1. Materials

Folic acid-poly(ethylene glycol)-conjugated cholesterol-grafted poly(glycerol adipate) (FPPC) was synthesized according to the previously published method [36]. Coumarin-6 (Sigma-Aldrich, St. Louis, MO, USA), curcumin (CUR, Xi'an Huarui Bio-Engineering Co., Ltd., Shaanxi, China), D- α -tocopheryl polyethylene glycol 1000 succinate (TPGS, BASF, Ludwigshafen, Germany), dimethyl sulfoxide (DMSO, Sigma-Aldrich, St. Louis, MO, USA), 3-(4,5-dimethylthiazol-2-yl)-2,5-diphenyltetrazolium bromide (MTT, AppliChem GmbH, Darmstadt, Germany), resveratrol (RV, Tokyo Chemical Industry Co., Ltd., Chuo-ku, Tokyo, Japan), and sterile water for injection (General Hospital Products. Public Co., Ltd., Pathumthani, Thailand) were employed as received. Methanol (high-performance liquid chromatography, HPLC, grade), acetonitrile (HPLC grade), and acetone (AR grade) were purchased from Honeywell Burdick & Jackson, Muskegon, MI, USA. Phosphate buffered saline (PBS), fetal bovine serum (FBS), penicillin-streptomycin, and trypsin 0.25%-ethylenediaminetetraacetic acid (trypsin-EDTA) were obtained from Life Technologies Corporation, Eugene, OR, USA. Dulbecco's modified Eagle's medium (DMEM, high glucose with sodium pyruvate), Alexa Fluor™ 647 Phalloidin, and Hoechst 33342 were bought from Invitrogen™, Thermo Fisher Scientific Inc., Waltham, MA, USA.

Saos-2 osteosarcoma cell lines (ATCC number HTB-85™, American Type Culture Collection, Manassas, VA, USA) were kindly provided by Prof. Pakpoom Kheolamai, Thammasat University, Pathumthani, Thailand. Primary dermal fibroblasts from normal human adults (ATCC number: PCS-201-012™) were purchased from American Type Culture Collection, Manassas, VA, USA. Both cells were cultured in DMEM supplemented with 10% FBS and 1% penicillin-streptomycin under 5% CO₂ humidified condition at 37 °C.

2.2. Preparation of nanoparticles

The NPs were prepared using the nanoprecipitation technique [36]. FPPC (5 mg) was dissolved in 4 ml of acetone. For drug-loaded NPs, CUR (0.05, 0.1, and 0.5 mg), RV (0.5, 1, and 1.5 mg), and CUR:RV at mass ratios of 1:1, 1:2, and 1:3 (equivalent to 0.5:0.5, 0.5:1, and 0.5:1.5 mg, respectively) were added to the polymeric solution. The solution was added drop by drop to 4 ml of the aqueous phase containing TPGS (5 mg) under continuous magnetic stirring. The mixture was magnetically stirred while the solvent evaporated under reduced pressure for 2 h. The resultant NP dispersion was collected for further analysis. For coumarin-6-loaded NPs used in the cellular uptake study, coumarin-6 was added to the polymeric solution instead of drugs, and the rest of the procedure was similarly performed as with drug-loaded NPs.

2.3. Characterization of nanoparticles

2.3.1. Determination of particle size, polydispersity index, and zeta potential

Particle size, polydispersity index (PDI), and zeta potential (ZP) of NPs were determined using Zetasizer NanoZS (Malvern Instrument Ltd., Malvern, UK) at an angle of 173°, a wavelength of 633 nm, and 25 °C. The measurements were performed in triplicate without sample dilution.

2.3.2. Determination of drug loading and entrapment efficiency

The loading efficiency of NPs was examined in terms of drug loading (DL) and entrapment efficiency (EE) through direct and indirect methods [36,38]. For the direct method, the NPs were dried in a desiccator until a constant weight was achieved and the weight of dried NPs was recorded. Subsequently, 100 μ l of DMSO was added to the dried NPs, followed by 15 min of sonication. Methanol (900 μ l) was then added, mixed, and sonicated for an additional 15 min. The resulting

mixture was centrifuged at 12,000 rpm for 15 min, and the supernatant was collected for further dilution and analysis by HPLC. For the indirect method, 400 μ l of NPs was added to a centrifugal filter unit (Amicon® Ultra, MWCO 3 kDa, Merck KGaA, Darmstadt, Germany) and centrifuged at 12,000 rpm for 15 min. The filtrate was collected and analyzed by HPLC to determine untrapped drugs. The entrapped drug in NPs was calculated as the difference between the total amount of drug determined by the direct method and the untrapped drug analyzed by the indirect method. The DL and EE were calculated according to equations (1) and (2), respectively.

$$DL (\%) = \frac{\text{Analyzed amount of entrapped drug in NPs}}{\text{Actual weight of dried NPs}} \times 100 \quad (1)$$

$$EE (\%) = \frac{\text{Analyzed amount of entrapped drug in NPs}}{\text{Initial amount of drug added}} \times 100 \quad (2)$$

2.3.3. Morphological examination

The morphology of NPs was investigated using a transmission electron microscope (TEM). The NPs were diluted two-fold in sterile water, air-dried on a formvar-coated grid, and stained with 1% uranyl acetate before the measurement. TEM images were captured by JEOL JEM-1400 (JEOL Ltd., Tokyo, Japan) with a TEM beam current at an accelerating voltage of 80 kV.

2.3.4. HPLC analysis

The quantitation of CUR and RV was conducted using the HPLC method, as previously described [32], with minor modifications. The HPLC analysis was carried out using a Prominence HPLC machine (Shimadzu Corporation, Kyoto, Japan) equipped with a diode array detector. The drugs were eluted through a reverse phase Phenomenex Gemini C18 column (4.6 mm \times 250 mm, 5 μ m) with a guard column at a flow rate of 1 ml/min. The mobile phase consisted of 50% v/v sterile water containing 1% v/v methanol and 0.01% v/v phosphoric acid as an aqueous phase, and 50% v/v acetonitrile as an organic phase. CUR and RV were detected at wavelengths of 430 and 320 nm, respectively. The system was validated over a concentration range of 0.1–50 μ g/ml for both drugs.

2.4. In vitro release study

The release of CUR and RV from NPs was investigated using the dialysis method in PBS pH 7.4, containing 1% sodium dodecyl sulfate (SDS) and 0.02% sodium azide, as a release medium. SDS and sodium azide were used to maintain a sink condition and prevent microbial growth, respectively. Two milliliters of NPs were added to a dialysis bag (MWCO 3.5 kDa, Cellu-Sep® T, Seguin, TX, USA). Subsequently, the dialysis bag was immersed in 10 ml of release medium and incubated at 100 rpm and 37 °C. At predetermined time intervals (0, 1, 2, 4, 6, 20, 24, 48, 72, 96, and 120 h), 1 ml of release medium was taken and immediately replaced with an equal volume of fresh release medium. The amounts of CUR and RV in the samples were then analyzed by HPLC. Additionally, the release of CUR and RV solutions, with equivalent amounts of drugs to those in NPs, was investigated to determine the impact of the dialysis membrane on the release of both drugs.

2.5. Nanoparticle stability study

Two stability assessments were conducted: 1) storage stability, and 2) NP stability upon dilution with different diluents. In both studies, the NPs were kept at ambient temperature (approximately 30 °C) and shielded from light. The physical stability of NPs was evaluated using Zetasizer NanoZS. To ascertain storage stability, the stability of undiluted NPs stored for 30 d were determined based on particle size, PDI, and ZP. For dilution stability, the physical stability of NPs diluted in PBS and normal saline solution (NSS) was assessed in terms of particle size,

PDI, and derived count rate, both immediately after dilution and following storage for 1 and 7 d. The measurements were conducted in triplicate using three independent samples.

2.6. Cytotoxicity test and synergism analysis of drug combination

The toxicity of drug solutions and drug-loaded NPs against Saos-2 cells was investigated for 48 h using a MTT assay [38]. The toxicity of the most potent drug-loaded NPs was also studied in PCS-201-012 cells, representing normal cells. Saos-2 and PCS-201-012 cells were seeded at a density of 2000 and 3000 cells/well, respectively, in 96-well plates. The cells were incubated at 37 °C in a 5% CO₂ humidified incubator for 24 h before adding samples. The samples were diluted to a predesigned concentration range in the culture medium and then incubated with the cells. After 48 h of incubation, the MTT solution was added and incubated for an additional 2 h. Subsequently, the medium was discarded, and DMSO (100 μ l) was added and incubated for 15 min before an absorbance measurement by Tecan's Infinite® 200 NanoQuant microplate reader (Männedorf, Switzerland) at a wavelength of 570 nm. Cell viability was calculated, and an IC₅₀ value was computed using GraphPad® Prism 7 software (GraphPad Software Inc., Boston, MA, USA). The MTT assay was performed in two experiments. The first experiment was to screen the toxicity of CUR (0.01–50 μ g/ml) and RV (5–120 μ g/ml) solutions to determine IC₅₀ ratios of CUR and RV for a synergistic study. The latter experiment was to investigate the toxicity and synergism of the combinations in both the solution and NP forms compared with their individual counterparts. The synergism of drug combination was determined by the combination index (CI)-isobologram equation [42,43]. The concentrations of CUR and RV combinations were adjusted based on their IC₅₀ values. CI values were calculated using CompuSyn software (ComboSyn, Inc., Paramus, NJ, USA). On a theoretical basis, the combinations possess synergistic, additive, and antagonistic effects when CI < 1, = 1, and >1, respectively.

2.7. Cell cycle assay

The cell cycle distribution of Saos-2 cells was examined using flow cytometry [38]. Cells were seeded in a 6-well plate at a density of 3 \times 10⁵ cells/well, incubated for 24 h, and treated with the samples for 24 and 48 h. The cells were harvested after trypsinization, washed with PBS, and fixed with cold ethanol for 2 h at 4 °C. After washing with ice-cold PBS, the cells were then stained with a cell cycle assay kit (Sigma-Aldrich Co. LLC., St. Louis, MO, USA) according to the manufacturer's protocol. The percentage of cell populations in each phase was measured using BD FACSVerse™ flow cytometer (BD Biosciences, Franklin Lakes, NJ, USA). The measurement was performed in three independent experiments.

2.8. Apoptosis assay

The apoptosis of cells after treatment with the drugs or drug-loaded NPs was determined using flow cytometry [38]. Saos-2 cells were seeded in a 6-well plate at a density of 3 \times 10⁵ cells/well and cultured for 24 h under the previously described condition. The cells were treated with a predefined concentration of samples for 24–48 h. After trypsinization, the cell pellets were collected and stained with a FITC Annexin V apoptosis detection kit I (BD Pharmingen™, BD Biosciences, Franklin Lakes, NJ, USA) according to the manufacturer's protocol. Measurement of viable, apoptotic, and necrotic cells was performed using BD FACSVerse™ flow cytometer (BD Biosciences, Franklin Lakes, NJ, USA). The experiments were conducted in triplicate.

2.9. Cellular uptake study

The quantitative uptake of NPs by Saos-2 cells was carried out using flow cytometry according to the previously published protocol [38] with

some modifications. Cells were seeded in a 12-well plate at a density of 2×10^5 cells/well and incubated for 24 h. Subsequently, the cells were incubated with coumarin-6-loaded NPs at concentrations of 62.5, 125, and 250 $\mu\text{g}/\text{ml}$. After 1- and 4-h of incubations, the cells were washed with PBS, trypsinized, and fixed with 4% paraformaldehyde. Fluorescence intensity was measured using a flow cytometer (BD FACSVerser™, BD Biosciences, Franklin Lakes NJ, USA). The uptake efficiency was reported as the mean fluorescence intensity per cell count. For the competitive uptake study, cells were incubated with 1 mM free folic acid solution (FFA) for 30 min before adding samples. The rest of the procedure was performed as previously described.

For the qualitative uptake study, cells were seeded in a poly(L-lysine)-precoated μ -slide 8-well high glass bottom (ibidi GmbH, Grafelfing, Germany) at a density of 8×10^4 cells/well. After 24 h, the cells were treated with 125 $\mu\text{g}/\text{ml}$ coumarin-6-loaded NPs for 1 h. Then, the cells were gently washed with pre-warmed PBS and fixed with 4% paraformaldehyde at room temperature for 30 min. The treatment of cells before measurement was performed at room temperature and protected from light, as follows; cells were incubated with 0.1% Triton-X/PBS solution for 3 min, then with 1% bovine serum albumin, stained with Alexa Fluor 647 for 30 min, and finally stained with Hoechst 33342 for 30 min. Cellular imaging was conducted using a confocal laser scanning microscope at $20 \times$ Plan-Apochromat (Zeiss LSM 900, Carl Zeiss AG, Oberkochen, Germany). The nucleus and cytoskeleton of the cells were visualized using 405 and 640 nm lasers at excitation/emission wavelengths of 348/455 and 653/668 nm, respectively. For coumarin-6-loaded NPs, a 488 nm laser with excitation and emission wavelengths of 456 and 500 nm, respectively, was utilized.

2.10. Statistical analysis

The data are presented as mean \pm standard deviation (S.D.) from at least three independent measurements. Paired and multiple comparisons were conducted using one-way ANOVA with the Scheffe test applied post hoc, respectively. The statistical analyses were performed using IBM® SPSS® statistics version 21 software (IBM Corporation, Armonk, NY, USA) for all aspects except for the release profiles. Repeated measure ANOVA was employed to compare the release profiles of all formulations using GraphPad® Prism 7 software (GraphPad Software Inc., Boston, MA, USA). A *p*-value of 0.05 or less was considered statistically significant.

3. Results and discussion

3.1. Synergism assay of CUR and RV solutions

To determine the synergistic ratio of CUR and RV, toxicity screening of CUR and RV was studied using MTT assay. Based on preliminary results from three independent experiments (Table S1), the IC_{50} ratios of

CUR and RV were calculated to be 1:2.2, 1:3.0, and 1:5.2, which were adjusted to 1:2, 1:3, and 1:5, respectively, and used for the synergistic assessment of Saos-2 cell viability. It is worth noting that these different CUR:RV ratios were obtained by fixing the amount of CUR and varying the amount of RV by 2-, 3-, and 5-fold, respectively. In this assay, CUR and RV solutions alone were used for comparison. The cell viability results versus the two-fold gradient concentrations of the three different CUR:RV ratios are shown as three-dimensional graphs (Fig. 1A). Increasing the amount of RV in the CUR:RV combination from 1:2 to 1:5 decreased the viability of Saos-2 cells. The fraction-affected (Fa)-CI correlations are shown in Fig. 1B. All CUR:RV combinations had CI values less than 1.0, suggesting a synergistic effect of the combinations. CI values less than 1.0 were found over the total concentration range of 7.5–30 $\mu\text{g}/\text{ml}$ for 1:2, 10–40 $\mu\text{g}/\text{ml}$ for 1:3, and 7.5–60 $\mu\text{g}/\text{ml}$ for 1:5 ratios. Considering the individual concentrations of CUR and RV within these ranges, the combinations exhibited synergism when they were composed of 2.5–10 $\mu\text{g}/\text{ml}$ CUR and 5–50 $\mu\text{g}/\text{ml}$ RV. However, this synergistic effect was primarily dependent on CUR concentration. Other RV doses within its investigated range, such as 20 $\mu\text{g}/\text{ml}$ CUR and 40 $\mu\text{g}/\text{ml}$ RV, did not show synergism. Therefore, the synergistic effect of CUR and RV was likely limited to a specific CUR concentration range. Within the specific synergistic range, the lowest CI value (approximately 0.5) was found for the 1:3 CUR:RV combination, whereas the 1:5 combination had the highest CI value (Table S2). The 1:3 CUR:RV combination exhibited synergism, with CI values within the range of 0.3–0.7 [44–46]. However, other ratios exhibited various levels of synergism. The toxicities of CUR, RV, and their combinations are summarized in Table 1. When the cells were treated with the individual drug solutions, the IC_{50} values of CUR and RV were 6.1 ± 3.8 and 31.7 ± 7.1 $\mu\text{g}/\text{ml}$, respectively. The IC_{50} values of CUR in the combinations were 0.6–1.1 folds lower than that of CUR alone, whereas those of RV in the combinations were 2–3 times lower than those of pure RV. Based on these results, the CUR:RV combinations synergistically potentiated anticancer effects,

Table 1

Half-maximal inhibitory concentrations (IC_{50}) of Saos-2 cells after treatment with CUR, RV, and their combinations (CUR:RV) at mass ratios of 1:2, 1:3, and 1:5.

	IC_{50} ($\mu\text{g}/\text{ml}$)	
	CUR	RV
CUR	6.1 ± 3.8	–
RV	–	31.7 ± 7.1
CUR:RV 1:2	7.0 ± 0.2	13.9 ± 0.4
CUR:RV 1:3	3.7 ± 1.4	$11.2 \pm 4.1^*$
CUR:RV 1:5	3.4 ± 0.9	16.9 ± 4.6

*Significant difference when comparing the values of groups treated with the combination and their individual. Data represents mean \pm S.D. from three experiments.

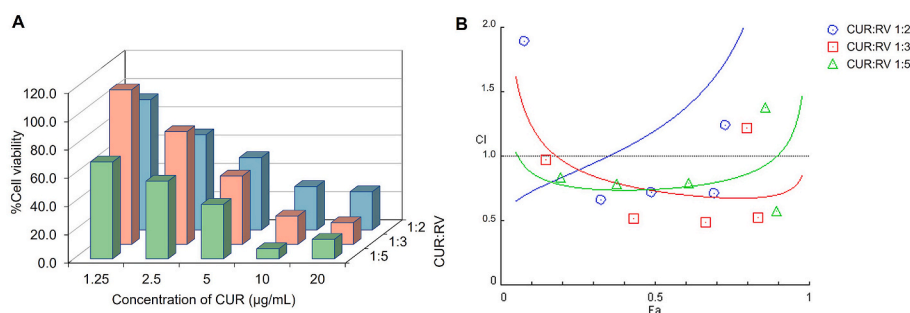


Fig. 1. (A) Cell viability of Saos-2 cells after 48 h of exposure to different combinations of curcumin (CUR) and resveratrol (RV) solutions at ratios of 1:2, 1:3, and 1:5. Data are presented as the mean \pm S.D. from triplicate experiments. (B) Fraction-affected (Fa)-combination index (CI) plot generated using CompuSyn 2.0 version for Saos-2 cells after treatment with 1:2, 1:3, and 1:5 ratios of CUR and RV combinations. The data plot represents the average values of each combination from three independent experiments.

even at a low amount of RV. Hence, 1:2 and 1:3 CUR:RV combinations were chosen for co-encapsulation into NPs.

3.2. Nanoparticle preparation for entrapment of CUR and RV combination

The NPs were fabricated using a nanoprecipitation method. FPPC, a folic acid-conjugated PEGylated PGA polymer, was incorporated into the organic phase. Ten NP formulations were prepared. The physical characteristics, drug loading, and entrapment efficiency of all NP formulations are summarized in Table 2. The blank NPs had a mean particle size of 100 ± 21 nm, PDI of 0.237 ± 0.119 , and ZP of -20.1 ± 5.4 mV. CUR entrapment was initially investigated by varying the ratio of CUR to FPPC (0.1:10, 0.5:10, and 1:10; Table 2). All CUR NPs had a particle size range of 85–109 nm, PDI of 0.108–0.114, and ZP of -25.1 to -27.4 mV. Compared to the blank NPs, all CUR NPs exhibited comparable particle sizes but significantly narrower size distributions and more negative ZP. The presence of CUR may enhance the hydrophilic-hydrophobic balance of polymeric chains [47]. In addition, the entrapped CUR was likely located inside the core of the NPs because of its hydrophobic nature, and accumulated in the hydrophobic cholesterol pendent near the glycerol groups of FPPC. CUR localization in the NP core may have disturbed the packing arrangement of FPPC and stretched the FOL-PEG chain out of the NPs, a phenomena that has been observed in CUR-loaded liposomes [28,48]. Loading CUR into the NPs resulted in particles with a narrow size distribution and a more negative surface charge. Among all CUR formulations, the smallest size and most negative ZP were observed for CUR-0.5 NPs because of the highly compacted and condensed core of the NPs at this ratio. The %DL increased with an increase in the initial amount of CUR; however, the %EE remained more or less constant. The highest %DL was obtained for CUR-1 NPs. Increasing the initial amount of CUR beyond a CUR:FPPC ratio of 1:10 resulted in the aggregation of NPs (data not shown), likely due to attaining the maximum loading capacity of the system. The maximum loading capacity is limited by the space in the polymer hydrophobic core, which acts as a loading region for lipophilic molecules [47,49]. Formulations with a high amount of drug moiety beyond the maximum loading capacity could cause breakdown of the particle structure and expose the excess drug to the aqueous phase. Therefore, the CUR-1 NPs were selected for further investigation. The morphological image of CUR-1 NPs showed a spherical shape with a layer of a hydrophilic shell, as indicated by the arrow in Fig. 2A.

Based on the synergy results, two combination ratios of CUR to RV (1:2 and 1:3, respectively) were chosen. The amount of RV in the formulations had to be equal to or greater than that of CUR. Therefore, to

study the effect of various amounts of RV and their combination on the particle characteristics, CUR:RV ratios of 1:1, 1:2, and 1:3 were employed to prepare co-loaded NPs and compared to individual RV-loaded NPs at an equivalent RV loading. For pairing with CUR:RV NPs, three different RV NPs were prepared with RV:FPPC ratios of 1:10 (RV-1), 2:10 (RV-2), and 3:10 (RV-3).

Comparing the individual RV-loaded NP properties to blank NPs, all RV NPs had larger sizes, a slightly narrower PDI, and comparable ZP values. An increase in the initial amount of RV increased the particle size and broadened the PDI, whereas the ZP became slightly more negative. A previous study demonstrated that RV is inserted and positioned between the headgroups of di-palmitoyl phosphatidylcholine, resulting in changes in headgroup orientation in the hydrophilic layer and chain packing in the hydrophobic core [50]. When the initial amount of RV increased, the NPs enlarged because more RV was preferentially located in the hydrophilic layer, which coincided with partial localization in the core. The highest %DL and %EE were $8.9 \pm 1.8\%$ and $97.9 \pm 19.4\%$, respectively, in RV-2 NPs. A further increase in the RV:FPPC ratio to 3:10 (RV-3 NPs) led to significant reductions in the %DL and %EE along with the formation of aggregates. In this case, the NPs reached capacity limitation at a RV:FPPC ratio of 2:10. As previously described, exceeding the maximum drug loading capacity and disrupting the hydrophilic/hydrophobic properties of the system can lead to non-entrapment of the drug and breakdown of the NP structure upon formation [47], resulting in a non-uniform size and lower drug loading. When comparing CUR-1 and RV-1 NPs, whose initial loading amounts were equal, both nanocarriers had comparable particle sizes and PDI values. However, RV-1 NPs exhibited a significantly less negative ZP and lower %EE and %DL than CUR-1 NPs. Because RV is less lipophilic than CUR, it may preferably be located at or near the surface of the NPs, and a lower number of RV molecules are entrapped in the hydrophobic particle core. The insertion of RV into the hydrophilic layer of the NPs led to a change in ZP. The TEM images (Fig. 2B) illustrate that RV NPs had a round shape but a thinner outer shell than CUR NPs, confirming the localization of RV in the hydrophobic core and hydrophilic shell of the NPs.

For CUR:RV NPs, the loading of CUR and RV combinations at 1:1, 1:2, and 1:3 ratios slightly affected the particle size. Compared with the blank NPs, none of the ratios altered the NPs size; however, the size distribution was reduced and the absolute ZP value was considerably increased by approximately 6–9 mV. Different ratios of CUR and RV did not significantly affect the NP properties. All CUR:RV NPs had particle ranging from 100 to 115 nm, PDI values from 0.117 to 0.131, and ZP values from -26.2 to -29.2 mV. Considering CUR content, the %DL slightly decreased, but the %EE was similar to that of the individual CUR-loaded NPs (CUR-1 NPs). As %DL was calculated based on the solid

Table 2

Particle size, polydispersity index (PDI), zeta potential (ZP), %drug loading (%DL), and %entrapment efficiency (%EE) of CUR-, RV-, and CUR:RV-loaded NPs.

Formulation code	Mass ratios			Size (nm)	PDI	ZP (mV)	%DL		%EE	
	CUR	RV	FPPC				CUR	RV	CUR	RV
Blank	–	–	10	100 ± 21	0.237 ± 0.119	-20.1 ± 5.4	–	–	–	–
CUR-0.1	0.1	–	10	101 ± 16	$0.108 \pm 0.019^{**}$	-25.1 ± 3.4	0.7 ± 0.1	–	84.1 ± 12.2	–
CUR-0.5	0.5	–	10	$85 \pm 3^*$	$0.114 \pm 0.013^{**}$	$-27.4 \pm 1.2^{**}$	2.1 ± 0.4	–	85.7 ± 12.2	–
CUR-1	1	–	10	109 ± 1	$0.109 \pm 0.019^{**}$	$-25.5 \pm 0.7^{**}$	$4.1 \pm 0.4^*$	–	88.2 ± 8.6	–
RV-1	–	1	10	108 ± 1	0.088 ± 0.004	-16.0 ± 0.9^s	–	3.7 ± 0.1	–	77.7 ± 1.2
RV-2	–	2	10	$119 \pm 1^{**}$	0.133 ± 0.025	-22.6 ± 5.0	–	8.9 ± 1.8^{ss}	–	97.9 ± 19.4
RV-3	–	3	10	$124 \pm 1^{**}$	0.266 ± 0.118^{ss}	-22.3 ± 2.2	–	6.2 ± 0.9	–	47.5 ± 6.9^{sss}
CUR:RV 1:1	1	1	10	100 ± 1	0.131 ± 0.009	$-27.9 \pm 1.8^{#***}$	3.5 ± 0.0	$3.5 \pm 0.1^{***}$	77.8 ± 1.1	77.5 ± 1.3
CUR:RV 1:2	1	2	10	115 ± 11	$0.117 \pm 0.023^{**}$	$-26.2 \pm 2.1^{**}$	3.8 ± 1.7	$8.3 \pm 0.4^{***}$	87.1 ± 14.4	99.6 ± 8.0
CUR:RV 1:3	1	3	10	110 ± 8	$0.121 \pm 0.022^{#***}$	$-29.2 \pm 2.9^{#***}$	3.6 ± 1.4	$11.3 \pm 2.6^{#***}$	89.8 ± 13.8	$95.5 \pm 16.0^{\#}$

*Significant difference when compared with other CUR NPs.

**Significant difference when compared with the blank NPs.

***Significant difference when comparing among other CUR:RV NPs.

^sSignificant difference when compared with other RV NPs.

^{ss}, ^{sss}Significant difference when compared with RV-1 and RV-2 NPs, respectively.

[#]Significant difference when compared with their corresponding single RV-loaded NPs at an equivalent drug:polymer ratio.

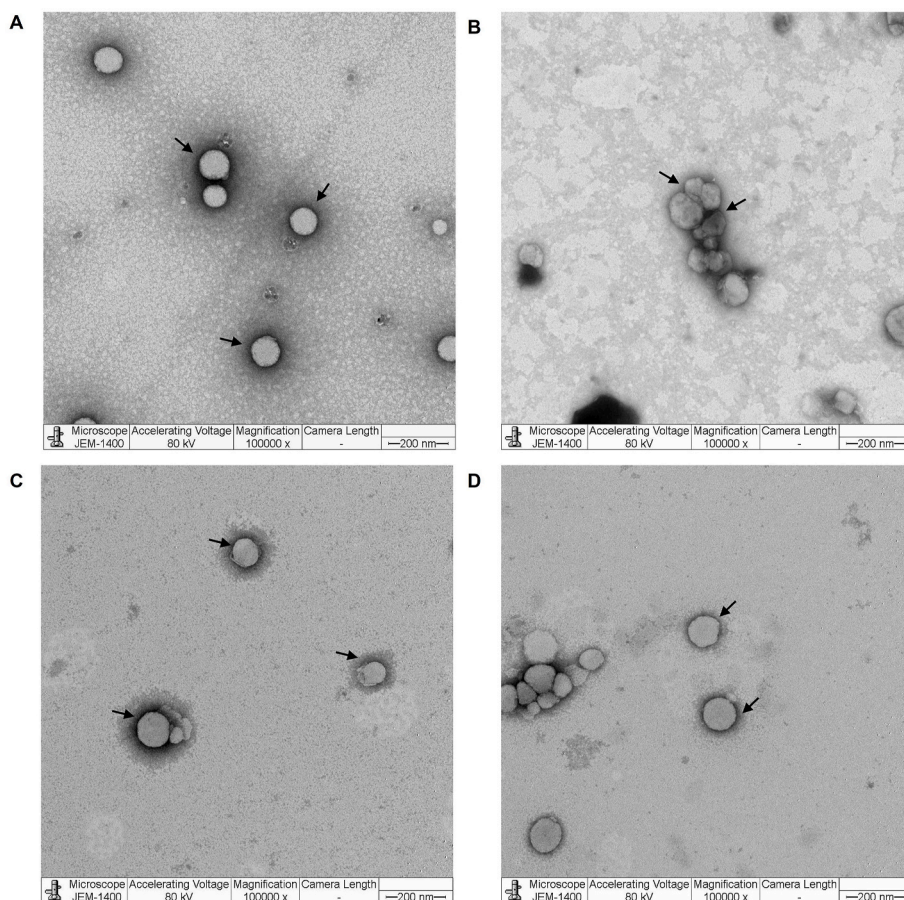


Fig. 2. TEM photographs of NPs: (A) CUR-1 NPs; (B) RV-2 NPs; (C) CUR:RV 1:2 NPs; and (D) CUR:RV 1:3 NPs. Arrows indicate the NP corona shell. Scale bars represent 200 nm.

content of the formulations, adding RV to the formulations resulted in a higher solid content, leading to a decrease in %DL. Increasing the CUR:RV ratio did not affect %DL, but tended to increase %EE. Regarding the RV content, %DL significantly increased with the initial amount of RV (p -value < 0.05), and %EE tentatively increased. The %EE of all the CUR:RV NPs was greater than 90% except for that of CUR:RV 1:1 NPs. Compared with the individual RV-loaded NPs at the equivalent amounts of drug added, the %EE of RV in CUR:RV NPs was not different, except for CUR:RV 1:3 NPs, which had a significantly higher %EE than RV-3 NPs. Comparing CUR:RV 1:3 NPs with CUR-1 NPs and RV-3 NPs, the particle size, PDI, and ZP of CUR:RV 1:3 NPs were similar to those of CUR-1 NPs, but their PDI and ZP differed from those of RV-3 NPs. Owing to the greater lipophilicity of CUR, its insertion into the core of the

particles was attributed to its hydrophobic compatibility with the cholesterol moiety of FPPC. In contrast, RV was located partially in the core but preferably in the hydrophilic layer of the NPs. The location of RV was further confirmed using TEM (Fig. 2C and D). The CUR:RV NPs were spherical and surrounded by corona shells, similar to CUR-1 and RV-2 NPs. However, CUR:RV 1:2 NPs had a thicker outer shell than CUR:RV 1:3 NPs, suggesting that a higher amount of RV was added to the latter and localized at or near the surface of the NPs. Co-loading of CUR and RV significantly improved the %DL and %EE of RV, possibly because of the interactions between CUR and RV upon particle formation. Therefore, the interactions between CUR and RV were examined by ATR-IR spectroscopy (Fig. 3). Blended mixtures of CUR and RV at mass ratios of 1:1, 1:2, and 1:3 were prepared, analyzed, and compared with

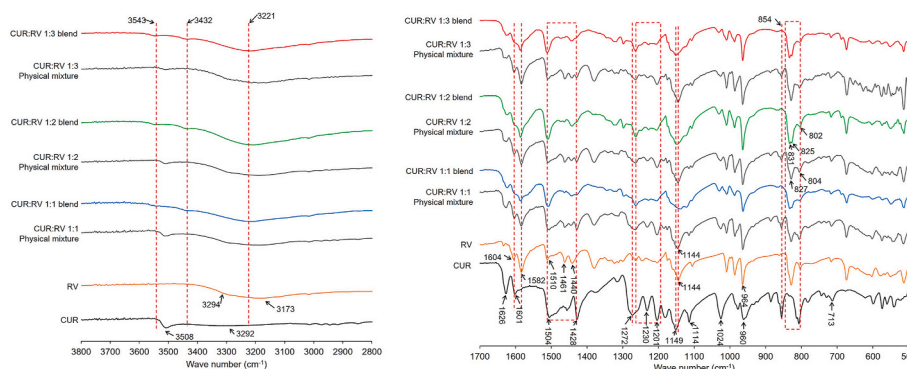


Fig. 3. ATR-IR spectra of CUR, RV, and their physical and blended mixtures at mass ratios of 1:1, 1:2, and 1:3.

their physical mixtures. The O–H stretching peaks of CUR at 3508 and 3292 cm^{-1} were attributed to intramolecular and intermolecular hydrogen bonding, respectively. CUR vibrations were observed at 1626 cm^{-1} (mixed C=C and C=O stretching), 1601 cm^{-1} (symmetric aromatic C=C_{ring} stretching), and 1504 cm^{-1} (C=O stretching, and C=C–C and C–C=O in-plane bending) [51]. The characteristic peaks of enol C–O bending, C–O–C bending, benzoate *trans*-CH vibration, and *cis*-CH vibration of the aromatic ring appeared at 1272, 1024, 959, and 713 cm^{-1} , respectively. The peak at 1149 cm^{-1} corresponded to the in-plane bending of aromatic CCH and skeletal CCH. In the case of pure RV, the characteristic aromatic C=C_{ring} stretching occurred at 1604 cm^{-1} , olefinic C=C stretching at 1582 cm^{-1} , in-plane C–H bending at 1510 and 1440 cm^{-1} , and C–O stretching of the phenol group at 1144 cm^{-1} . The out-of-plane C–H bending of RCH=CHR was observed at 966 cm^{-1} , indicating a typical *trans*-configuration of RV [52,53].

Interestingly, the CUR and RV blend exhibited a prominent shift in the characteristic peaks of the individual molecules. The O–H stretching peaks of CUR at 3508 and 3292 cm^{-1} shifted and split to 3543 and 3432 cm^{-1} ; meanwhile, a change in O–H stretching peak patterns of CUR at 3292 cm^{-1} and RV at 3297 and 3173 cm^{-1} was observed, and the new peak pattern occurred at 3221 cm^{-1} . In addition, the C=O stretching peaks of CUR at 1504 cm^{-1} and RV at 1510 cm^{-1} merged, and the peak pattern over the region of 1485–1500 cm^{-1} altered from that of the physical mixture [54]. The shift in these peaks suggests hydrogen bonding between CUR and RV. In addition to hydrogen bonding, hydrophobic interactions also occurred between CUR and RV. The aromatic C–H out-of-plane bending peak of CUR at 854 cm^{-1} vanished, and that of RV at 827 cm^{-1} shifted to 831 cm^{-1} with a new peak appearance at 825 cm^{-1} . The peak intensities of the aromatic C=C_{ring} of CUR at 1601 cm^{-1} and the aromatic C=C of RV at 1604 cm^{-1} diminished. The change in peak pattern over the 1510–1460 cm^{-1} region corresponding to aromatic ring stretching and in-plane C–H bending occurred [54]. The olefinic C=C stretching peak at 1582 cm^{-1} slightly shifted to 1584 cm^{-1} , and the peak at 1272 cm^{-1} belonging to in-plane C–H bending of C=CH and aromatic C–O stretching disappeared. Regarding the ATR-IR spectra of the physical mixtures of CUR and RV at all ratios, the frequency and pattern of all typical peaks of CUR and RV did not change, with a decrease in the peak intensity because of the dilution effect of various ratios of the mixtures. These changes in the aromatic fingerprint patterns imply hydrophobic interactions between CUR and RV through van der Waals forces or π - π stacking. These interactions did not change the *trans*-configuration of RV based on the unchanged frequency and intensity of the peak at 964 cm^{-1} . Based on the interaction study, it can be concluded that the enhanced loading efficiency of CUR:RV NPs proceeded through hydrogen bonding and hydrophobic interactions between CUR and RV.

3.3. *In vitro* drug release profiles

The release of CUR and RV from NPs was studied using a dialysis method. CUR-1 NPs, RV-2 NPs, CUR:RV 1:2 NPs, and CUR:RV 1:3 NPs were used to investigate CUR and RV release patterns compared with equivalent amounts of CUR and RV solutions. Over 80% of the CUR and RV solutions were rapidly released into the release medium (PBS pH 7.4) within the first 8 h, as illustrated in Fig. 4A and B, respectively, suggesting that the dialysis bag did not affect the release of these molecules. All the NPs slowly released CUR in a sustained manner for 120 h. Indifferent release rates of CUR were observed for all CUR-containing NPs. Within 120 h, 43.42–44.63% CUR release was achieved. The presence of RV in the formulation did not influence the release rate of CUR except for the lag time. An increase in the amount of RV in the NPs led to a decrease in the lag time of CUR release. As shown in Fig. 4A, CUR-1 NPs began to release the drug after 4 h of incubation, whereas the initial release of CUR from CUR:RV 1:2 and 1:3 NPs was observed at 2 and 1 h, respectively.

Regarding the release of RV from the NPs (Fig. 4B), approximately 80% of RV was rapidly released from all NP formulations within the first 24 h because of the localization of RV in the outer hydrophilic layer of the NPs, as previously described, and its hydrophilic nature [33,55]. All NPs had similar initial release profiles, as shown in Fig. 4B, regardless of RV loading. The final extent of RV release tentatively depended on RV loading; at the end of the experiment, $75.50 \pm 0.54\%$ and $78.72 \pm 4.56\%$ RV were released from RV-2 NPs and CUR:RV 1:2 NPs, respectively, whereas $80.66 \pm 0.45\%$ was released from CUR:RV 1:3 NPs. The presence of CUR in the formulation did not affect the release pattern or rate of RV from NPs.

From the release profiles of CUR and RV, CUR and RV co-loading did not affect the release rate and extent of CUR but altered its lag time. The decrease in lag time was attributed to the hydrophilic properties of RV, leading to more water penetration into the particle core and accelerating CUR diffusion from the particle core. Although CUR and RV interacted, these interactions did not affect the release rate and extent of CUR. It is possible that the weak interactions between CUR and RV proceeded through hydrophobic or π - π stacking interactions, without the formation of strong complexes. Taken together, because of the favorable localization of RV in the hydrophilic shell, the occurrence of CUR-RV interactions facilitated the localization of CUR in the outer shell and the penetration of water molecules into the NP core. This phenomenon accelerated the initial release of CUR from NPs and reduced the lag time. This finding demonstrates the influence of the co-loaded drugs on individual release profiles. RV, a hydrophilic drug, potentially accelerates the release of hydrophobic CUR upon co-encapsulation. This allows tailoring of the initial drug release rates in co-delivery systems to potentially match the desired synergistic effect at the target site, which requires further investigation.

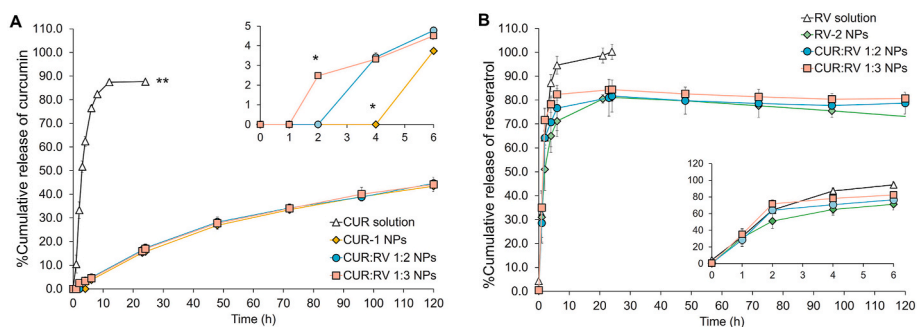


Fig. 4. Release profiles of (A) curcumin (CUR) and (B) resveratrol (RV) from CUR-1 NPs, CUR:RV 1:2 NPs, CUR:RV 1:3 NPs, and RV-2 NPs in comparison with CUR and RV solutions ($n = 3$). An inset illustrates the release profiles within the first 6 h

*Significant difference among the NP formulations; and **significant difference between the NP formulations and their corresponding solutions.

3.4. Stability study

Despite the fact that NPs show favorable biological performance in an *in vitro* model, their stability can be a challenge. Polymeric NPs are promising delivery systems for anticancer agents. However, their clinical translation is hindered by particle aggregation [56]. Furthermore, NPs containing anticancer drugs that are intended for intravenous administration generally require dilution with different diluents before administration. The type, pH, and ionic strength of the diluents may affect the physical stability of the NPs [57]. Therefore, particle stability is a concern for ensuring product stability and patient safety. In this study, changes in the particle size, PDI, and ZP of stock NPs when stored at ambient temperature for 30 d, were used to determine their storage stability. Moreover, the physical stability of the NPs upon dilution in three diluents (SWI, PBS, and NSS) was investigated. Changes in particle size, PDI, and ZP are graphically illustrated in Fig. 5A-C. The particle sizes of all NPs remained unchanged over 30 d of storage at ambient temperature. Their size distributions were comparable to the initial values, except for CUR:RV 1:2 NPs, which increased from 0.116 ± 0.021 to 0.143 ± 0.014 . Although there were some fluctuations in their distribution during storage, the PDI values of all the formulations were less than 0.200 at the end of the experiment, suggesting a narrow size distribution. The surface charge of CUR-1 NPs was stable over 30 d. However, the ZP of the NPs containing RV was altered upon storage. The surface charge of RV-2 NPs gradually became more negative, possibly because of the leakage of RV from the particle core. In contrast, the ZP of CUR:RV 1:2 NPs slightly increased, while that of CUR:RV 1:3 NPs drastically shifted to less negative values due to neutralization, possibly caused by particle-particle agglomeration or interaction with the medium [58].

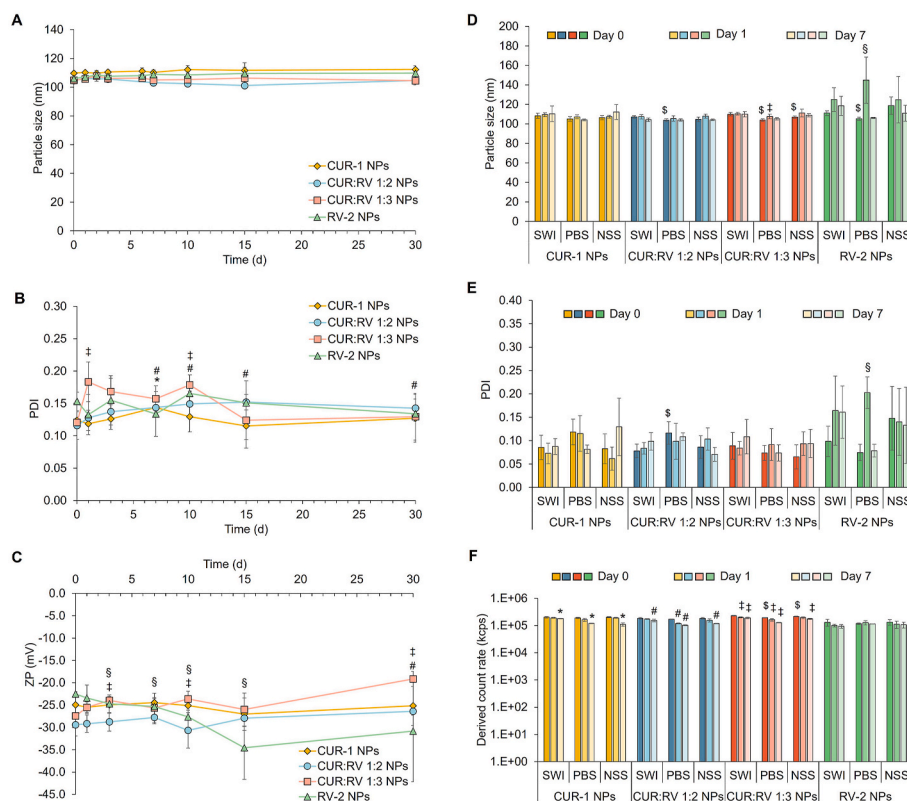


Fig. 5. (A–C) Storage stability profiles of CUR-1 NPs, CUR:RV 1:2 NPs, CUR:RV 1:3 NPs, and RV-2 NPs when stored at ambient temperature for 30 d. (D–F) Physical stability of CUR-1 NPs, CUR:RV 1:2 NPs, CUR:RV 1:3 NPs, and RV-2 NPs upon 10-fold dilution in SWI, PBS, and NSS and stored at ambient temperature for 7 d. The characteristics of NPs were evaluated in terms of particle size (A and D), polydispersity index (PDI, B and E), zeta potential (ZP, C), and derived count rate (F). *, #, †, § Significant difference when comparing the values of CUR-1 NPs, CUR:RV 1:2 NPs, CUR:RV 1:3 NPs, and RV-2 NPs, respectively, at any time with those on day 0; and § significant difference between the value in PBS or NSS and that in SWI.

The physical stability of the NPs upon dilution in SWI, PBS, and NSS is summarized in Fig. 5D-F. The particle sizes of all NPs remained stable in PBS and NSS compared to SWI. The size distribution of all NPs in these diluents was below 0.150. The derived count rate values were similar to those of particles in SWI. Considering these minimal changes, the NPs were considered stable in PBS and NSS after dilution. When these diluted NPs were stored for 1 and 7 d, the particle sizes of CUR-1, CUR:RV 1:2, and CUR:RV 1:3 NPs exhibited slight alterations, and their PDI values were below 0.120. However, PBS had an adverse effect on the stability of RV-2 NPs, whose size and PDI increased after a day of storage, although no large aggregates were observed in the distribution histograms (Fig. S1). Storing the diluted NPs for 7 d resulted in a gradual decrease in the derived count rate of all NPs. An upward trend in the count rate implies particle aggregation, whereas a decline in the count rate indicates either NP sedimentation or dissociation [59,60]. Taking into account the particle size and PDI data, the decreased derived count rate can be attributed to NP sedimentation or dissociation. PBS and NSS had minimal effects on the stability of all NPs. Except for RV-2 NPs, all NPs were stable for at least 1 d after dilution in PBS and NSS. The instability of RV-2 NPs may be associated with the localization of RV in the outer shell of the NPs, and further investigation is needed to understand the mechanisms underlying their destabilization. However, prolonged storage for 7 d may lead to physical instability of the NPs.

3.5. Cytotoxicity and synergistic effect of CUR- and RV-co-loaded NPs

The toxicities of CUR:RV 1:2 and CUR:RV 1:3 NPs were evaluated and compared with those of CUR-1 and RV-2 NPs. The results are shown in Fig. 6. In comparison with pure compounds, CUR-1 NPs and RV-2 NPs had 1.4–3.6 times lower IC_{50} values ($4.4 \pm 1.8 \mu\text{g/ml}$ and $8.9 \pm 1.6 \mu\text{g/}$

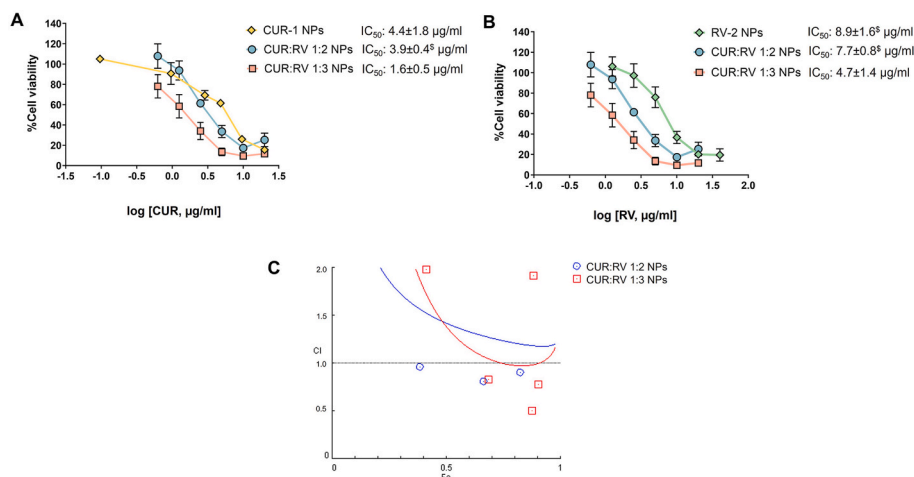


Fig. 6. Cell viability of Saos-2 cells and IC₅₀ values of (A) CUR and (B) RV after treatment with CUR-1 NPs, RV-2 NPs, CUR:RV 1:2 NPs, and CUR:RV 1:3 NPs for 48 h. (C) Fraction-affected (Fa)-combination index (CI) plot generated using CompuSyn 2.0 version for Saos-2 cells after treatment with CUR:RV 1:2 NPs and CUR:RV 1:3 NPs for 48 h. Data are presented as the mean ± S.D. from three independent experiments.

[§]Significant difference between the value of NPs and that of their corresponding free drugs.

ml, respectively), than their corresponding solutions, suggesting that NPs enhanced the anticancer effect of CUR and RV. The co-loaded NPs had IC₅₀ values of CUR and RV by 1.8–3.6 times lower than the individual compounds. CUR:RV 1:2 NPs had slightly smaller IC₅₀ values than CUR-1 NPs and RV-2 NPs, while a dramatic decrease in IC₅₀ values by 1.9–2.8 times was observed in the case of CUR:RV 1:3 NPs. The CI

values of CUR:RV 1:2 and CUR:RV 1:3 NPs were below 1.0 (Fig. 6C). The CUR:RV 1:3 NPs had lower CI values than CUR:RV 1:2 NPs. This result is consistent with the synergistic effect of their combinations in free drug form (Fig. 1B). To confirm the safety of the most potent CUR:RV NPs, CUR:RV 1:3 NPs were selected to test their toxicity in PCS-201-012 cells (primary dermal fibroblasts from normal human adults). The IC₅₀ values

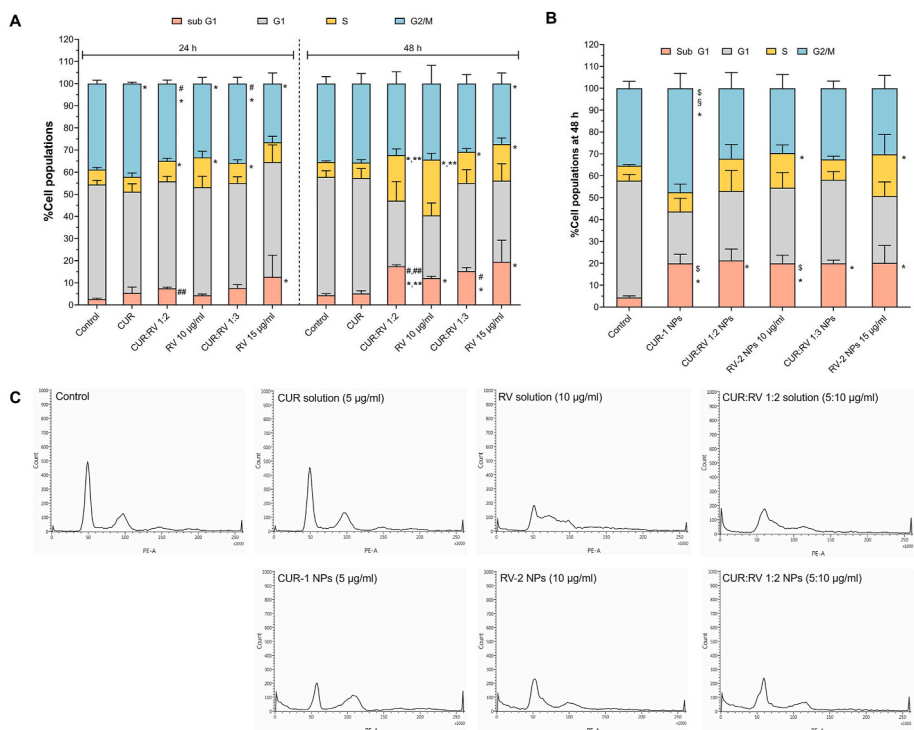


Fig. 7. Cell cycle analysis presented as percentages of Saos-2 cell populations distributed in each phase after treatment with the solutions of CUR (5 µg/ml), RV (10 and 15 µg/ml), and their combinations at ratios of 1:2 and 1:3 (5:10 and 5:15 µg/ml, respectively) for 24 and 48 h. Data are presented as the mean ± S.D. (n = 3). (B) Saos-2 cell cycle distribution after treatment with CUR-1 NPs (5 µg/ml), RV-2 NPs (10 and 15 µg/ml), CUR:RV 1:2 NPs (5:10 µg/ml), and CUR:RV 1:3 NPs (5:15 µg/ml) for 48 h. Data are presented as the mean ± S.D. (n = 3). (C) Exemplified cell cycle profiles after 48 h of treatment with drug-loaded NPs and their corresponding solutions.

*Significant difference between the treated group and the control group; **significant difference between the value at 24 h and that at 48 h; # significant difference between the combination-treated group and the CUR-treated groups; ## significant difference between the combination-treated group and the RV-treated group (CUR:RV 1:2 vs RV 10 µg/ml and CUR:RV 1:3 vs RV 15 µg/ml); § significant difference between the value of NPs and that of their corresponding free drugs; §§ significant difference among the other NP formulations; ns insignificant difference compared with RV-2 NPs (15 µg/ml).

of CUR and RV were 3.4 ± 0.1 and 10.0 ± 0.2 $\mu\text{g}/\text{ml}$, respectively. These values demonstrated lower toxicity to normal cells than to osteosarcoma cells. These findings suggest that the synergistic effect of CUR and RV was preserved upon encapsulation in the NPs, thereby enhancing their anticancer effects even when the drugs were individually or dually loaded into the NPs.

3.6. Effects on cell cycle and apoptosis profiles

3.6.1. Effect on cell cycle profiles

The effects of CUR and RV loaded NPs on the Saos-2 cell cycle were investigated using flow cytometry and compared with those of their corresponding solutions. The effect of CUR solution on G2/M phase accumulation was marginal at 24 h, and disappeared when the incubation time was extended to 48 h ($p > 0.05$) (Fig. 7A). There was no change in the S and sub G1 phases when Saos-2 cells were treated with CUR solution. When CUR was incorporated into NPs (CUR-1 NPs, Fig. 7B), a significant increase in the G2/M phase of the cells ($47.56 \pm 6.82\%$) was observed at 48 h, compared to the control ($35.42 \pm 3.15\%$) and CUR solution ($35.68 \pm 4.55\%$). In addition, CUR-1 NPs dramatically increased the sub G1 phase of the cells ($p < 0.05$). This suggests an induction of G2/M phase accumulation and an increase in cell death when CUR was encapsulated in NPs. The cell distribution pattern in the CUR-1 NP-treated group was noticeably different from that in the group treated with CUR solution, as shown in Fig. 7C.

The S phase populations of RV solution-treated cells increased over time (Fig. 7A), accompanied by a reduction in the G2/M population and an increase in the sub G1 population. The higher concentration of RV solution ($15 \mu\text{g}/\text{ml}$) decreased the S phase populations but induced the sub G1 accumulation when compared to lower RV concentration ($10 \mu\text{g}/\text{ml}$). This result implies that a higher concentration of RV caused more cell death than a lower concentration through S phase arrest. Regarding the effect of RV-2 NPs at 48 h (Fig. 7B), these nanocarriers at 10 and $15 \mu\text{g}/\text{ml}$ increased the S phase populations to $15.85 \pm 3.74\%$ and $19.10 \pm 9.05\%$, respectively, compared to the control group ($6.80 \pm 0.52\%$). These populations were comparable to those in the groups treated with RV solution. However, RV-2 NPs significantly increased sub G1 phase cells, suggesting increased cell death when RV was incorporated into NPs. Notably, further increasing the concentration of RV-2 NPs to $15 \mu\text{g}/\text{ml}$ did not increase the cells in this phase. The cell cycle distribution patterns of all the RV-treated groups were drastically different from those of the control group (Fig. 7C). In addition, the pattern of the NP-treated group differed slightly from that of the solution-treated group.

When CUR and RV were combined at ratios of 1:2 and 1:3 ratios as solutions, the S and sub G1 populations of the treated cells increased with incubation time (Fig. 7A). Both combined solutions induced a lower accumulation of the S phase population than RV alone, whereas no accumulation of the G2/M phase was observed. A significant increment in sub G1 populations compared to single drug treatment was observed following treatment with the 1:2 combination for 48 h. When the cells were incubated with the co-loaded NPs for 48 h (Fig. 7B), CUR:RV 1:2 and CUR:RV 1:3 NPs slightly increased the cell populations in the S phase ($14.77 \pm 6.60\%$ and $9.32 \pm 1.43\%$, respectively) compared to the control group. CUR:RV 1:2 NPs had a greater impact on S phase populations than the CUR:RV 1:3 combination. The population in the sub G1 phase gradually increased to $21.32 \pm 5.20\%$ and $19.99 \pm 1.44\%$ with CUR:RV 1:2 and CUR:RV 1:3 NP treatments, respectively, compared to their corresponding solutions ($17.44 \pm 0.67\%$ and $15.27 \pm 1.67\%$, respectively). Similar patterns of cell cycle distribution were observed in the CUR:RV NPs- and CUR:RV solution-treated groups (Fig. 7C). The data at 24 h of incubation (Table S3) showed that CUR:RV 1:3 NPs increased the S and sub G1 phase populations to $11.61 \pm 5.63\%$ and $10.82 \pm 3.99\%$, respectively. An extended exposure period of 48 h increased the sub G1 population of the cells after treatment with CUR:RV 1:3 NPs to $19.99 \pm 1.44\%$, while the S phase slightly declined to $9.32 \pm 1.43\%$. This result suggests that CUR:RV 1:3 NPs induced sub G1

phase accumulation in Saos-2 cells, leading to cell death after longer exposure times. Incorporating CUR and RV into NPs significantly increased the sub G1 population compared to the other phases of the cell cycle. The percentages of sub G1 cells after treatment with CUR:RV NPs at both ratios were not significantly different from those of CUR-1 and RV-2 NPs and did not increase cell populations in the G2/M phase.

3.6.2. Effect on apoptosis profiles

The apoptotic results of CUR and RV solutions are shown in Fig. 8A. The solutions ($5 \mu\text{g}/\text{ml}$ and $10 \mu\text{g}/\text{ml}$, respectively) slightly caused cell apoptosis compared to the control group, whereas increasing RV concentration to $15 \mu\text{g}/\text{ml}$ induced more apoptosis. The apoptotic rates after 48 h of exposure to the 1:2 and 1:3 CUR:RV combined solutions ($32.94 \pm 1.07\%$ and $31.27 \pm 3.54\%$, respectively) were higher than those of cells treated with pure CUR ($20.76 \pm 3.00\%$) and RV ($21.49 \pm 2.05\%$ and $28.52 \pm 5.16\%$ for 10 and $15 \mu\text{g}/\text{ml}$, respectively) solutions. The 1:3 combination increased apoptosis at 24 h of incubation, whereas the 1:2 combination had a more pronounced effect later.

The apoptosis results after treatment with NPs are presented in Fig. 8B. Incorporating CUR and RV into NPs increased late apoptosis of the cells by 2–11% compared to their corresponding free drug solutions. The quadratic patterns of cells treated with NPs differed from those of cells treated with the drug solutions (Fig. 8C), especially in late apoptosis (upper right quadrant). The population of cells treated with NPs in this quadrant was higher than for those treated with the solutions, indicating a greater late apoptotic population of cells after NP treatment. This was attributed to the efficient delivery of CUR and RV into cells by the NPs, surpassing the efficacy of free drugs and leading to increased cell death. When comparing the co-loaded NPs to the individual drug-loaded NPs, the overall percentage of apoptotic cells after treatment with the former ($35.06 \pm 3.31\%$ and $48.39 \pm 4.07\%$ for CUR:RV 1:2 and 1:3 NPs, respectively) was comparable to the corresponding individual drug-loaded NPs ($34.55 \pm 2.55\%$, $30.53 \pm 6.75\%$, and $48.29 \pm 3.40\%$ for CUR-1 NPs, $10 \mu\text{g}/\text{ml}$ RV-2 NPs, and $15 \mu\text{g}/\text{ml}$ RV-2 NPs, respectively). Regarding late apoptosis, the cell population slightly increased after treatment with CUR:RV 1:2 NPs ($26.41 \pm 3.67\%$) compared to $10 \mu\text{g}/\text{ml}$ RV-2 NPs ($21.75 \pm 3.51\%$), but it was comparable to that of CUR-1 NPs ($27.46 \pm 0.66\%$). However, CUR:RV 1:3 NPs ($33.84 \pm 1.28\%$) significantly increased late apoptosis compared to CUR-1 NPs and $15 \mu\text{g}/\text{ml}$ RV-2 NPs ($29.35 \pm 0.91\%$). The increased late apoptosis and sub G1 populations were a result of the more efficient delivery of CUR and RV into the cells by NPs, accelerating cell deaths. This finding aligns well with the cytotoxicity data.

In previous reports, CUR and RV were chosen to induce apoptosis in cancer cells in association with cell cycle arrest [1,2]. CUR and RV induce cell death via various mechanisms involving the cell cycle, apoptosis, and inflammation. Depending on its concentration, CUR regulates cell cycle arrest in the G1/S or G2/M phases, [61,62]. Previous studies have demonstrated CUR-induced time- and concentration-dependent cell cycle arrest in human osteosarcoma [61, 62]. Herein, the cells were arrested in the G1/S phase at an earlier incubation time and subsequently blocked in the G2/M phase at a later time. In addition, a relatively low dose of CUR accumulated cells in the G1/S phase, whereas a higher dose induced accumulation in the G2/M phase before apoptosis. Our results showed that CUR alone rarely affected the cell cycle distribution and apoptosis of Saos-2 cells, possibly because the tested concentration was ineffective. When CUR was incorporated into NPs, it considerably increased the accumulation of Saos-2 cells in the G2/M phase. Other research has reported that α -tocopherol succinate (TOS) in the concentration range of 20–40 μM induces Saos-2 cell accumulation in the S/G2 phase, coinciding with a decrease in G1 cell populations without any effect on cell proliferation [63]. The observed increase in the G2/M fraction of Saos-2 cells treated with CUR-1 NPs could be attributed to either enhanced CUR accumulation in the cells facilitated by the NPs, or the effect of TOS present in the form of TPGS within the formulation. RV is involved in S

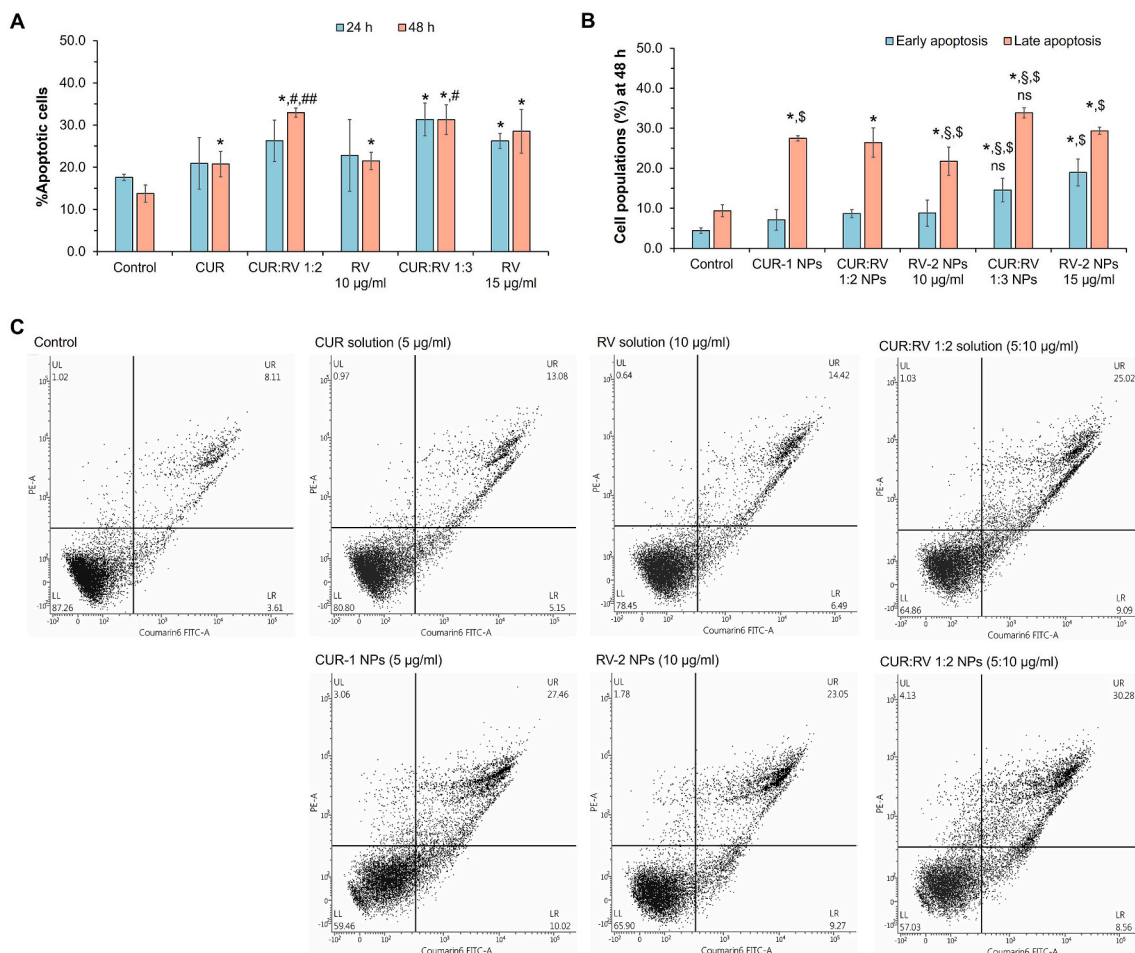


Fig. 8. Apoptosis assay presented as percentages of Saos-2 cell populations. (A) Percentages of total apoptotic cells after treatment with the solutions of CUR (5 µg/ml), RV (10 and 15 µg/ml), and their combinations at ratios of 1:2 and 1:3 (5:10 and 5:15 µg/ml, respectively) for 24 and 48 h. Data are presented as the mean ± S.D. (n = 3). (B) Percentages of early and late apoptosis of Saos-2 cells after treatment with CUR-1 NPs (5 µg/ml), RV-2 NPs (10 and 15 µg/ml), CUR:RV 1:2 NPs (5:10 µg/ml), and CUR:RV 1:3 NPs (5:15 µg/ml) for 48 h. Data are presented as the mean ± S.D. (n = 3). (C) Examples of apoptotic profiles after 48 h of treatment with drug-loaded NPs and their corresponding solutions. Each quadrant shows viable (lower left), necrotic (upper left), early apoptotic (lower right), and late apoptotic (upper right) cells.

*Significant difference between the treated group and the control group; #significant difference between the combination-treated group and the CUR-treated groups; ##significant difference between the combination-treated groups and the RV-treated group (CUR:RV 1:2 vs RV 10 µg/ml and CUR:RV 1:3 vs RV 15 µg/ml); §significant difference between the value of NPs and that of their corresponding free drugs; §§significant difference among the other NP formulations; nsinsignificant difference compared with RV-2 NPs (15 µg/ml).

phase-specific arrest and induces apoptosis, which causes cell death [64]. In this study, RV significantly induced S phase arrest in a time-dependent manner, which is consistent with previous reports in other cell lines [64,65]. Combined treatment with CUR and RV solutions predominantly regulated S phase arrest and induced apoptosis, causing more cell death than individual drug treatments. In the case of CUR:RV NPs and RV-2 NPs, more pronounced effects on the S phase of cell distribution than on the other phases was observed, despite containing an equivalent amount of TPGS to CUR-1 NPs. A previous study reported RV-induced S phase arrest in thyroid carcinoma cells [65]. However, it is worth noting that RV, in the concentration range of 10–20 µg/ml, induced G0/G1 phase accumulation in MG63 osteosarcoma cells, while it caused S phase arrest in Tel-1 esophageal and A431 epidermal cancer cells [64]. In the current study, RV-2 NPs induced S phase arrest without significant accumulation of cells in the G2/M and G1 phases. Interestingly, when CUR and RV were combined in NPs, they induced the sub G1 phase of cells, leading to increased cell deaths. This result suggests that the anticancer effect of the combination of CUR and RV in both the solution and NP forms was primarily due to the induction of apoptosis and, to some extent, cell cycle arrest.

3.7. Cellular uptake of NPs

To ensure that the administered NPs entered and localized in the cells, the uptake of NPs by Saos-2 osteosarcoma cells was investigated using coumarin-6-loaded FPPC NPs. The results are expressed as uptake efficiency in Fig. 9A. The uptake of NPs increased with the incubation time and NP concentration. FPPC NPs were prepared using folic acid-decorated PGA-based polymer and TPGS. It was anticipated that the NPs would enter cells through folate receptor-mediated endocytosis. Folic acid (FA) demonstrates a strong affinity for folate receptors [66] and facilitates uptake through endocytosis, which can be hindered by preincubating cells with free FA (FFA) in the medium. To explore the impact of FA-mediated cellular uptake, the competitive inhibition of FPPC NP uptake was studied by incubating cells with 1 mM FFA for 30 min before treatment with NPs. As shown in Fig. 9B, no reduction in percentage uptake was observed in the FFA-pretreated group. The competitive uptake of TPGS-free formulations was further investigated. The results revealed that 1 mM FFA partially inhibited NP uptake by approximately 20%. Based on these results, it was hypothesized that the presence of TPGS in the FPPC NP formulation might facilitate NP

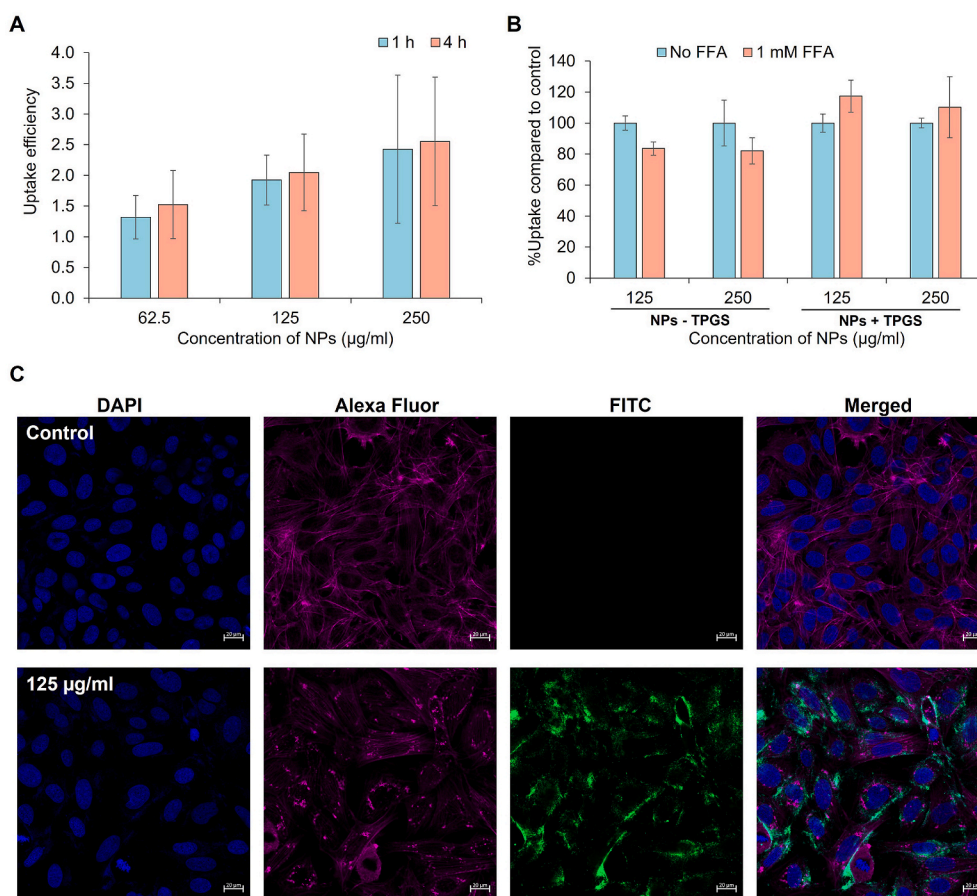


Fig. 9. (A) The uptake efficiency of coumarin-6-loaded NPs at 62.5, 125, and 250 µg/ml after incubation with Saos-2 cells for 1 and 4 h. (B) The uptake percentage of particles by Saos-2 cells in the free folic acid (FFA)-pretreated group in comparison with that in the control group without FFA pretreatment. The cells were pretreated with 1 mM FFA for 30 min before incubation with coumarin-6-loaded NPs with and without TPGS in the formulations. (C) CLSM images of Saos-2 cells after incubated with 125 µg/ml coumarin-6-loaded NPs for 1 h compared with the control group (untreated cells). The cells were captured in four channels: DAPI, Alexa Fluor, FITC, and merged images illustrate Hoechst 33342-stained nuclei, Alexa Fluor 647 phalloidin-stained F-actin, coumarin-6-loaded NPs, and overlaying of DAPI, Alexa Fluor, and FITC channels, respectively.

internalization through a FA-independent pathway, which requires further investigation.

NP localization within cells was examined using CLSM. The cells were incubated with 125 µg/ml coumarin-6-loaded NPs for 1 h and stained with Hoechst 33342 and Alexa Fluor 647 to observe the nucleus and cytoskeleton of the cells, respectively. As illustrated in Fig. 9C, the control (untreated cells) did not show green fluorescence in the FITC channel, suggesting that there was no autofluorescence in the cells in this channel. A green signal corresponding to coumarin-6 was clearly observed in the NP-treated cells. The merged channel did not show any change in the color of the signals corresponding to the co-localization of NPs and the cytoskeleton. A green signal was observed around the nuclei. These findings suggest that the NPs entered the cells and localized around the nucleus and cytoplasm.

These results confirmed the *in vitro* biological performance of the NPs; the toxicity of CUR and RV toward Saos-2 cells was enhanced and their synergistic effect was maintained following loading into FPPC NPs. The FPPC NPs delivered CUR and RV into the cells through endocytosis and subsequently caused sub G1 accumulation and apoptosis.

4. Conclusion

This study demonstrates the simultaneous delivery of CUR and RV encapsulated in folic acid-conjugated poly(glycerol adipate)-based NPs (FPPC NPs) to osteosarcoma cells. The loading efficiency of RV was positively influenced by co-encapsulation with CUR, owing to physical

interactions between the two molecules. However, the release profiles of CUR and RV were not mutually influenced by the formulation as NPs, except for the accelerated lag time of CUR release. The localization of RV within the NPs affected the NP morphology and thickness of the hydrophilic outer shell. The developed NPs maintained the synergistic effects of CUR and RV, and potentiated their anticancer activity against Saos-2 cells. The presence of TPGS in the formulation hindered cellular uptake of NPs through receptor-mediated endocytosis but did not affect the overall uptake efficiency of the system. The current study offers an initial proof-of-concept for a potential tumor-targeted co-delivery system of CUR and RV, which synergistically enhances their *in vitro* anticancer activity against osteosarcoma. This versatile drug delivery system has the potential to precisely co-encapsulate various therapeutic agents for synergistic combinations of other chemotherapeutic drugs with adjuvants for cancer vaccines, gene therapy, and immunotherapy. This platform may also be utilized in combinatorial medicine for a wide range of diseases where a co-encapsulation strategy is needed. Although further *in vivo* studies are required, this study paves the way for a potentially transformative therapy for cancer treatment using nanoparticulate drug delivery systems. This platform may be applicable as an alternative treatment for osteosarcoma in the future, which may overcome drug-related side effects and treatment failure associated with conventional chemotherapy.

Funding

This research project is supported by Mahidol University (Basic Research Fund: fiscal year 2022 [Project no. BRF1-032/2565]). VT would like to thank the University of Nottingham for his Nottingham Research Fellowship.

ORCID authorship contribution statement

Amaraporn Wongrakpanich: Writing – review & editing, Writing – original draft, Validation, Supervision, Methodology, Investigation, Formal analysis, Conceptualization. **Huong Bui Thi Thu:** Writing – review & editing, Investigation, Formal analysis. **Krisada Sakchaisri:** Writing – review & editing, Validation, Supervision, Methodology, Investigation, Formal analysis, Conceptualization. **Vincenzo Taresco:** Writing – review & editing, Validation, Methodology, Investigation, Funding acquisition, Formal analysis. **Valentina Cuzzucoli Crucitti:** Writing – review & editing, Validation, Methodology, Investigation, Formal analysis. **Somnuk Bunsupa:** Writing – review & editing, Validation, Supervision, Methodology, Investigation, Formal analysis, Conceptualization. **Jiraphong Suksiriworapong:** Writing – review & editing, Writing – original draft, Validation, Supervision, Project administration, Methodology, Investigation, Funding acquisition, Formal analysis, Conceptualization.

Declaration of competing interest

The authors declare that they have no known competing financial interests or personal relationships that could have appeared to influence the work reported in this paper.

Data availability

Data will be made available on request.

Acknowledgements

This research project is supported by Mahidol University (Basic Research Fund: fiscal year 2022 [Project no. BRF1-032/2565]). We would like to thank Prof. Dr. Pakpoom Kheolamai, Division of Cell Biology, Faculty of Medicine, Thammasat University for kindly giving Saos-2 osteosarcoma cell lines. VT would like to thank the University of Nottingham for his Nottingham Research Fellowship.

Appendix A. Supplementary data

Supplementary data to this article can be found online at <https://doi.org/10.1016/j.jddst.2024.105610>.

References

- B.L. Tan, M.E. Norhaizan, Curcumin combination chemotherapy: the implication and efficacy in cancer, *Molecules* 24 (14) (2019) 2527.
- Q. Xiao, W. Zhu, W. Feng, S.S. Lee, A.W. Leung, J. Shen, et al., A review of resveratrol as a potent chemoprotective and synergistic agent in cancer chemotherapy, *Front. Pharmacol.* 9 (2019) 1534.
- S.C. Gupta, S. Patchva, B.B. Aggarwal, Therapeutic roles of curcumin: lessons learned from clinical trials, *AAPS J.* 15 (1) (2013) 195–218.
- S. Prasad, S.C. Gupta, A.K. Tyagi, B.B. Aggarwal, Curcumin, a component of golden spice: from bedside to bench and back, *Biotechnol. Adv.* 32 (6) (2014) 1053–1064.
- S. Patra, B. Pradhan, R. Nayak, C. Behera, L. Rout, M. Jena, et al., Chemotherapeutic efficacy of curcumin and resveratrol against cancer: chemoprevention, chemoprotection, drug synergism and clinical pharmacokinetics, *Semin. Cancer Biol.* 73 (2021) 310–320.
- K.-H. Lu, P.W.-A. Lu, E.W.-H. Lu, C.-W. Lin, S.-F. Yang, Curcumin and its analogs and carriers: potential therapeutic strategies for human osteosarcoma, *Int. J. Biol. Sci.* 19 (4) (2023) 1241–1265.
- D.K. Walters, R. Muff, B. Langsam, W. Born, B. Fuchs, Cytotoxic effects of curcumin on osteosarcoma cell lines, *Invest. N. Drugs* 26 (4) (2008) 289–297.
- A. De Luca, D. Bellavia, L. Raimondi, V. Carina, V. Costa, M. Fini, et al., Multiple effects of resveratrol on osteosarcoma cell lines, *Pharmaceuticals* 15 (3) (2022) 342.
- L. Peng, D. Jiang, Resveratrol eliminates cancer stem cells of osteosarcoma by STAT3 pathway inhibition, *PLoS One* 13 (10) (2018) e0205918.
- Q. Du, B. Hu, H.M. An, K.P. Shen, L. Xu, S. Deng, et al., Synergistic anticancer effects of curcumin and resveratrol in Hepa1-6 hepatocellular carcinoma cells, *Oncol. Rep.* 29 (5) (2013) 1851–1858.
- L.I. Gavrilas, D. Cruceriu, C. Ionescu, D. Miere, O. Balacescu, Pro-apoptotic genes as new targets for single and combinatorial treatments with resveratrol and curcumin in colorectal cancer, *Food Funct.* 10 (6) (2019) 3717–3726.
- A.P. Majumdar, S. Banerjee, J. Nautiyal, B.B. Patel, V. Patel, J. Du, et al., Curcumin synergizes with resveratrol to inhibit colon cancer, *Nutr. Cancer* 61 (4) (2009) 544–553.
- N.K. Narayanan, D. Nargi, C. Randolph, B.A. Narayanan, Liposome encapsulation of curcumin and resveratrol in combination reduces prostate cancer incidence in PTEN knockout mice, *Int. J. Cancer* 125 (1) (2009) 1–8.
- A. Arena, M.A. Romeo, R. Benedetti, L. Masuelli, R. Bei, M.S. Gilardini Montani, et al., New insights into curcumin- and resveratrol-mediated anti-cancer effects, *Pharmaceuticals* 14 (11) (2021) 1068.
- L. Masuelli, E. Di Stefano, M. Fantini, R. Mattera, M. Benvenuto, L. Marzocchella, et al., Resveratrol potentiates the *in vitro* and *in vivo* anti-tumoral effects of curcumin in head and neck carcinomas, *Oncotarget* 5 (21) (2014) 10745–10762.
- T. Ramasamy, J.H. Kim, J.Y. Choi, T.H. Tran, H.-G. Choi, C.S. Yong, et al., pH sensitive polyelectrolyte complex micelles for highly effective combination chemotherapy, *J. Mater. Chem. B* 2 (37) (2014) 6324–6333.
- D. Wu, A. Pusuluri, D. Vogus, V. Krishnan, CWt Shields, J. Kim, et al., Design principles of drug combinations for chemotherapy, *J. Contr. Release* 323 (2020) 36–46.
- A. Di Paolo, G. Bocci, Drug distribution in tumors: mechanisms, role in drug resistance, and methods for modification, *Curr. Oncol. Rep.* 9 (2) (2007) 109–114.
- C.-M.J. Hu, L. Zhang, Nanoparticle-based combination therapy toward overcoming drug resistance in cancer, *Biochem. Pharmacol.* 83 (8) (2012) 1104–1111.
- C.-M.J. Hu, S. Aryal, L. Zhang, Nanoparticle-assisted combination therapies for effective cancer treatment, *Theor. Deliv. 1* (2) (2010) 323–334.
- R. Rathore, B.A. Van Tine, Pathogenesis and current treatment of osteosarcoma: perspectives for future therapies, *J. Clin. Med.* 10 (6) (2021).
- D. Chen, X. Liu, X. Lu, J. Tian, Nanoparticle drug delivery systems for synergistic delivery of tumor therapy, *Front. Pharmacol.* 14 (2023) 1111991.
- A. Eftekhari, C. Kryschi, D. Pamies, S. Gulec, E. Ahmadian, D. Janas, et al., Natural and synthetic nanovectors for cancer therapy, *Nanotheranostics* 7 (3) (2023) 236–257.
- A. Shaito, A.M. Posadino, N. Younes, H. Hasan, S. Halabi, D. Alhababi, et al., Potential adverse effects of resveratrol: a literature review, *Int. J. Mol. Sci.* 21 (6) (2020).
- R.A. Sharma, W.P. Steward, A.J. Gescher, Pharmacokinetics and pharmacodynamics of curcumin, *Adv. Exp. Med. Biol.* 595 (2007) 453–470.
- C. Guo, J. Yin, D. Chen, Co-encapsulation of curcumin and resveratrol into novel nutraceutical hyalurosomes nano-food delivery system based on oligo-hyaluronic acid-curcumin polymer, *Carbohydr. Polym.* 181 (2018) 1033–1037.
- M.M. Leena, T. Anukiruthika, J.A. Moses, C. Anandharamkrishnan, Co-delivery of curcumin and resveratrol through electrospayed core-shell nanoparticles in 3D printed hydrogel, *Food Hydrocolloids* 124 (2022) 107200.
- M. Huang, C. Liang, C. Tan, S. Huang, R. Ying, Y. Wang, et al., Liposome co-encapsulation as a strategy for the delivery of curcumin and resveratrol, *Food Funct.* 10 (10) (2019) 6447–6458.
- X. Chen, C. Yu, Y. Zhang, Y.-C. Wu, Y. Ma, H.-J. Li, Co-encapsulation of curcumin and resveratrol in zein-bovine serum albumin nanoparticles using a pH-driven method, *Food Funct.* 14 (7) (2023) 3169–3178.
- K. Coradini, R.B. Friedrich, F.N. Fonseca, M.S. Vencato, D.F. Andrade, C. M. Oliveira, et al., A novel approach to arthritis treatment based on resveratrol and curcumin co-encapsulated in lipid-core nanocapsules: *In vivo* studies, *Eur. J. Pharmacol. Sci.* 78 (2015) 163–170.
- K. Coradini, F.O. Lima, C.M. Oliveira, P.S. Chaves, M.L. Athayde, L.M. Carvalho, et al., Co-encapsulation of resveratrol and curcumin in lipid-core nanocapsules improves their *in vitro* antioxidant effects, *Eur. J. Pharm. Biopharm.* 88 (1) (2014) 178–185.
- L.J. Carlson, B. Cote, A.W. Alani, D.A. Rao, Polymeric micellar co-delivery of resveratrol and curcumin to mitigate *in vitro* doxorubicin-induced cardiotoxicity, *J. Pharmaceut. Sci.* 103 (8) (2014) 2315–2322.
- P. Saralkar, A.K. Dash, Alginate nanoparticles containing curcumin and resveratrol: preparation, characterization, and *in vitro* evaluation against DU145 prostate cancer cell line, *AAPS PharmSciTech* 18 (7) (2017) 2814–2823.
- Y. Zheng, R. Jia, J. Li, X. Tian, Y. Qian, Curcumin- and resveratrol-co-loaded nanoparticles in synergistic treatment of hepatocellular carcinoma, *J. Nanobiotechnol.* 20 (1) (2022) 339.
- S. Ben-Zichri, M. Meltzer, S. Lacham-Hartman, S. Kulusheva, U. Hadad, N. Papo, et al., Synergistic activity of anticancer polyphenols embedded in amphiphilic dendrimer nanoparticles, *ACS Appl. Polym. Mater.* 4 (12) (2022) 8913–8925.
- K. Damrongrak, K. Kloysawat, S. Bunsupa, K. Sakchaisri, A. Wongrakpanich, V. Taresco, et al., Delivery of acetogenin-enriched *Annona muricata* Linn leaf extract by folic acid-conjugated and triphenylphosphonium-conjugated poly (glycerol adipate) nanoparticles to enhance toxicity against ovarian cancer cells, *Int. J. Pharm.* 618 (2022) 121636.

- [37] A. Tchoryk, V. Taresco, R.H. Argent, M. Ashford, P.R. Gellert, S. Stolnik, et al., Penetration and uptake of nanoparticles in 3D tumor spheroids, *Bioconjugate Chem.* 30 (5) (2019) 1371–1384.
- [38] J. Suksiriworapong, C. Achayawat, P. Juangrattanajakorn, V. Taresco, V. C. Crucitti, K. Sakchaisri, et al., Modification of poly(glycerol adipate) with tocopherol and cholesterol modulating nanoparticle self-assemblies and cellular responses of triple-negative breast cancer cells to SN-38 delivery, *Pharmaceutics* 15 (8) (2023) 2100.
- [39] J. Suksiriworapong, N. Pongprasert, S. Bunsupa, V. Taresco, V.C. Crucitti, T. Janurai, et al., CD44-targeted lipid polymer hybrid nanoparticles enhance anti-breast cancer effect of *Cordyceps militaris* extracts, *Pharmaceutics* 15 (6) (2023) 1771.
- [40] V. Taresco, I. Tulini, I. Francolini, A. Piozzi, Polyglycerol adipate-grafted polycaprolactone nanoparticles as carriers for the antimicrobial compound usnic acid, *Int. J. Mol. Sci.* 23 (22) (2022) 14339.
- [41] P.L. Jacob, B. Brugnoli, A. Del Giudice, H. Phan, V.M. Chauhan, L. Beckett, et al., Poly (diglycerol adipate) variants as enhanced nanocarrier replacements in drug delivery applications, *J. Colloid Interface Sci.* 641 (2023) 1043–1057.
- [42] N. Zhang, J.N. Fu, T.C. Chou, Synergistic combination of microtubule targeting anticancer fludelonone with cytoprotective panaxytriol derived from panax ginseng against MX-1 cells *in vitro*: experimental design and data analysis using the combination index method, *Am. J. Cancer Res.* 6 (1) (2016) 97–104.
- [43] T.-C. Chou, P. Talalay, Quantitative analysis of dose-effect relationships: the combined effects of multiple drugs or enzyme inhibitors, *Adv. Enzym. Regul.* 22 (1984) 27–55.
- [44] T.C. Chou, The mass-action law based algorithm for cost-effective approach for cancer drug discovery and development, *Am. J. Cancer Res.* 1 (7) (2011) 925–954.
- [45] C. Watala, J. Wzorek, A. Palma, M. Boncler, A comparison of different regression models for the quantitative analysis of the combined effect of P2Y12 and P2Y1 receptor antagonists on ADP-induced platelet activation, *Thromb. Res.* 211 (2022) 88–97.
- [46] J.L. Hernández, L. Padilla, S. Dakhel, T. Coll, R. Hervas, J. Adan, et al., Therapeutic targeting of tumor growth and angiogenesis with a novel anti-S100A4 monoclonal antibody, *PLoS One* 8 (9) (2013) e72480.
- [47] A. Gupta, A.P. Costa, X. Xu, S.-L. Lee, C.N. Cruz, Q. Bao, et al., Formulation and characterization of curcumin loaded polymeric micelles produced via continuous processing, *Int. J. Pharm.* 583 (2020) 119340.
- [48] A. Krawiec, D. Bielska, B. Gzyl-Malcher, M. Kepczynski, R. Lach, M. Nowakowska, Interaction of curcumin with lipid monolayers and liposomal bilayers, *Colloids Surf. B Biointerfaces* 88 (1) (2011) 231–239.
- [49] S.C. Lee, K.M. Huh, J. Lee, Y.W. Cho, R.E. Galinsky, K. Park, Hydrotropic polymeric micelles for enhanced paclitaxel solubility: *In vitro* and *in vivo* characterization, *Biomacromolecules* 8 (1) (2007) 202–208.
- [50] A. de Ghellinck, C. Shen, G. Fragneto, B. Klösgen, Probing the position of resveratrol in lipid bilayers: a neutron reflectivity study, *Colloids Surf. B Biointerfaces* 134 (2015) 65–72.
- [51] P.R.K. Mohan, G. Sreelakshmi, C.V. Muraleedharan, R. Joseph, Water soluble complexes of curcumin with cyclodextrins: characterization by FT-Raman spectroscopy, *Vib. Spectrosc.* 62 (2012) 77–84.
- [52] M. Popova, A. Szegedi, V. Mavrodinova, N. Novak Tušar, J. Mihály, S. Klébert, et al., Preparation of resveratrol-loaded nanoporous silica materials with different structures, *J. Solid State Chem.* 219 (2014) 37–42.
- [53] F. Aghaz, Z. Asadi, S. Sajadimajd, K. Kashfi, E. Arkan, Z. Rahimi, Codelivery of resveratrol melatonin utilizing pH responsive sericin based nanocarriers inhibits the proliferation of breast cancer cell line at the different pH, *Sci. Rep.* 13 (1) (2023) 11090.
- [54] Coates J. Interpretation of infrared spectra, A practical approach. *Encycl. Anal. Chem.*
- [55] A.G. Muller, S.D. Sarker, A.A. Fatokun, G.A. Hutcheon, Formulation of resveratrol into PGA-co-PDL nanoparticles increases its cytotoxic potency against lung cancer cells. *RPS Pharmacy and, Pharmacol. Rep.* 2 (1) (2022).
- [56] A. Zielińska, F. Carreiró, A.M. Oliveira, A. Neves, B. Pires, D.N. Venkatesh, et al., Polymeric nanoparticles: production, characterization, toxicology and ecotoxicology, *Molecules* 25 (16) (2020) 3731.
- [57] Y. Ishikawa, Y. Katoh, H. Ohshima, Colloidal stability of aqueous polymeric dispersions: effect of pH and salt concentration, *Colloids Surf. B Biointerfaces* 42 (1) (2005) 53–58.
- [58] Z. Hussain, M. Pandey, H. Choudhury, P.C. Ying, T.M. Xian, T. Kaur, et al., Hyaluronic acid functionalized nanoparticles for simultaneous delivery of curcumin and resveratrol for management of chronic diabetic wounds: fabrication, characterization, stability and *in vitro* release kinetics, *J. Drug Deliv. Sci. Technol.* 57 (2020) 101747.
- [59] Manual, Zetasizer Nano Series User (Man0317-5.0), Malvern Instruments Ltd, Malvern, UK, 2004.
- [60] J. Suksiriworapong, V. Taresco, D.P. Ivanov, I.D. Styliari, K. Sakchaisri, V. B. Junyaprasert, et al., Synthesis and properties of a biodegradable polymer-drug conjugate: methotrexate-poly(glycerol adipate), *Colloids Surf. B Biointerfaces* 167 (2018) 115–125.
- [61] A. Hu, J.J. Huang, J.F. Zhang, W.J. Dai, R.L. Li, Z.Y. Lu, et al., Curcumin induces G2/M cell cycle arrest and apoptosis of head and neck squamous cell carcinoma *in vitro* and *in vivo* through ATM/Chk2/p53-dependent pathway, *Oncotarget* 8 (31) (2017) 50747–50760.
- [62] D.S. Lee, M.K. Lee, J.H. Kim, Curcumin induces cell cycle arrest and apoptosis in human osteosarcoma (HOS) cells, *Anticancer Res.* 29 (12) (2009) 5039–5044.
- [63] R. Alleva, M.S. Benassi, L. Pazzaglia, M. Tomasetti, N. Gellert, B. Borghi, et al., α -Tocopheryl succinate alters cell cycle distribution sensitising human osteosarcoma cells to methotrexate-induced apoptosis, *Cancer Lett.* 232 (2) (2006) 226–235.
- [64] J. Dun, X. Chen, H. Gao, Y. Zhang, H. Zhang, Y. Zhang, Resveratrol synergistically augments anti-tumor effect of 5-FU *in vitro* and *in vivo* by increasing S-phase arrest and tumor apoptosis, *Exp. Biol. Med.* (Maywood, NJ, U. S.) 240 (12) (2015) 1672–1681.
- [65] X.-M. Yu, R. Jaskula-Sztul, K. Ahmed, A.D. Harrison, M. Kunnimalaiyaan, H. Chen, Resveratrol induces differentiation markers expression in anaplastic thyroid carcinoma via activation of Notch1 signaling and suppresses cell growth, *Mol. Cancer Therapeut.* 12 (7) (2013) 1276–1287.
- [66] C. Marchetti, I. Palaia, M. Giorgini, C. De Medici, R. Iadarola, L. Vertechy, et al., Targeted drug delivery via folate receptors in recurrent ovarian cancer: a review, *OncoTargets Ther.* 7 (2014) 1223–1236.